

# Facile and Scalable Synthesis of Si@void@C Embedded in Interconnected Three-Dimensional Porous Carbon Architecture for High Performance Lithium Ion Batteries

Jingyun Ma\*, Hua Tan, Hong Liu\*, Yimin Chao\*

Dr. J. Ma

School of Materials Science and Engineering, Qilu University of Technology (Shandong Academy of Sciences), Jinan 250353, P. R. China

Dr. H. Tan and Prof. H. Liu

State Key Laboratory of Crystal Materials, Shandong University, Jinan 250100, P. R. China

Prof. Y. Chao

School of Chemistry, University of East Anglia, Norwich NR4 7TJ, United Kingdom

E-mail: mjy2003@qlu.edu.cn, hongliu@sdu.edu.cn, y.chao@uea.ac.uk

**Abstract** Si-based materials possess huge potential as an excellent anode material for Li-ion batteries. However, how to realize scalable synthesis of Si-based anode with a long cycling life and high-performance is still a critical challenge. Here we report a Water-in-Oil Microemulsion process followed by UV illumination, calcination and hydrothermal method to produce yolk-shell Si@void@C embedded in interconnected three-dimensional porous carbon network architecture using silicon nanoparticles. As a result, the sample Si@void@C/C-2 electrode has achieved a reversible capacity of 1160 mA h g<sup>-1</sup> at 0.2 A g<sup>-1</sup> after 300 cycles and a stable long cycling life of 480 mA h g<sup>-1</sup> at 1 A g<sup>-1</sup> after 1000 cycles. A full battery with the synthesized anode and LNMC cathode shows a capacity of 128 mA h g<sup>-1</sup> at 0.2 A g<sup>-1</sup> as well as good cycling stability after 1100th cycles. Such excellent electrochemical performance is ascribed to its unique structure, the yolk-shell void space, highly robust carbon shells and interconnected porous carbon nets, that can improve the conductivity of the electrode, buffer the volume expansion, and also suppress Si nanoparticles stress variation. This Water-in Oil system makes it possible for mass production of environmentally friendly synthesis of core - shell structure.

**Keywords:** Water-in-Oil Microemulsion, Si@void@C, interconnected porous carbon, anode, lithium ion batteries

## 1. Introduction

To meet the rapid development of portable powers for electronics and electric vehicles, the adventure of Lithium ion batteries (LIBs) require anode material with high energy density and low commercial costs Silicon, <sup>[1-3]</sup> with high theoretical specific capacity of 4200 mA h g<sup>-1</sup>, low working voltage and in abundance, has become the first choice of anode candidates in terms of high specific capacity among the extensive research work.<sup>[4,5]</sup> However, the low conductivity and huge volume change during charge/discharge process causing the appearance with solid electrolyte interphase (SEI), granular material pulverization and reduce the area of inter-particles electrical contact, which result in deteriorated electrochemical performance and impeded the large-scale commercialization of Si anode.<sup>[6]</sup> To solve the aforementioned issues, nanosized engineering has been used in practice with different nanostructured morphologies. Such as Si nanoparticles,<sup>[7]</sup> Si microsphere,<sup>[8]</sup> Si nanowires<sup>[9]</sup>, Si nanosheets<sup>[10]</sup> and porous hollow Si nanocubes<sup>[11]</sup> Nevertheless, the limited number of cycling stability from nanostructures cannot make Si anode prone to real application. Another effective strategy is to coat Si with oxides<sup>[12]</sup> metals<sup>[13]</sup> and conducting carbonaceous<sup>[14]</sup>, which can minimize the destruction of the electrode architecture by the volume change of individual particles as well as render a stable SEI on the surface of individual material particles thereby restraining the degradation of electron/lithium ion transport paths from/ to silicon.<sup>[15]</sup> Especially Si/C nanohybrids, the conducting carbonaceous and porous hollow nanostructure can enhance the transmission speed for electron and shorten the diffusion distance of Li<sup>+</sup>. Therefore, hybridizing silicon nanoparticles with void space and porous carbon nanomaterials, can improve the conductivity and make the best of the void space to alleviate the volume stress during the initial lithiation process.<sup>[16]</sup> For example, yolk-shell Si@void@C nanostructure can decrease the electrical resistance between Si yolks and hollow carbon shells, effectively buffer the huge volume variation of Si, and protect yolks from electrolyte corrosion.<sup>[17]</sup> Porous Si/C composites with buffering void synthesized by co-assembly of phenol formaldehyde resin process exhibit a high rate capability of 721 mA h g<sup>-1</sup> at 2A g<sup>-1</sup>.<sup>[18]</sup> However, the preparation process involves the use of silica, which is removed using strong corrosive HF solution. Chen et al has reported multilayered Si nanoparticles/reduced graphene oxide hybrid, which shows an outstanding

lithium storage performance with high reversible capacity of 2300 mA h g<sup>-1</sup> at 0.05 C.<sup>[19]</sup> Although these Si/C hybrid electrodes have good electrochemical cycling life, the synthesis processes have a series of shortcomings, such as expensiveness for large scale production, use of sophisticated equipment, low production yield and long synthesis time.<sup>[20-22]</sup> Realization of easy and scalable production of Si@void@C/C composites with the decent performance is a crucial step towards practical applications.

In this work, a novel architecture of yolk-shell Si@void@C nanoparticles embedded in three-dimensional (3-D) carbon-net has been prepared by Water-in-Oil micromulsion under UV illumination, calcination and hydrothermal methods. Void space and porous nanostructure were in situ grown among Si nanoparticles, carbon shells and interconnected carbon-net. The formation of specific nanostructure of Si@void@C/C is depended on the suitable UV illumination time for Water-in-Oil Micromulsion, which precisely stabilizes the structure upon lithiation, while the carbon shell and carbon-net in the composite ensures the electronic contact of silicon particles. Benefiting from the controlled processing parameter for the carbon, 3D porous structure of Si@void@C/C-2 with highly conductive porous networks and void space display outstanding electrochemical performance, superior to that pure silica, Si@void@C-1 and Si@void@C-3 samples. This synthesis approach possesses advantages of environmentally friendly, low cost, facile process, and easy to implement large-scale industrial production for Si@void@C/C to commercial use. This method also can be easily extended to the preparation of core-shell transition metal oxides/carbon, Sn/C materials, Ge/C materials and other porous carbon-based anode materials.

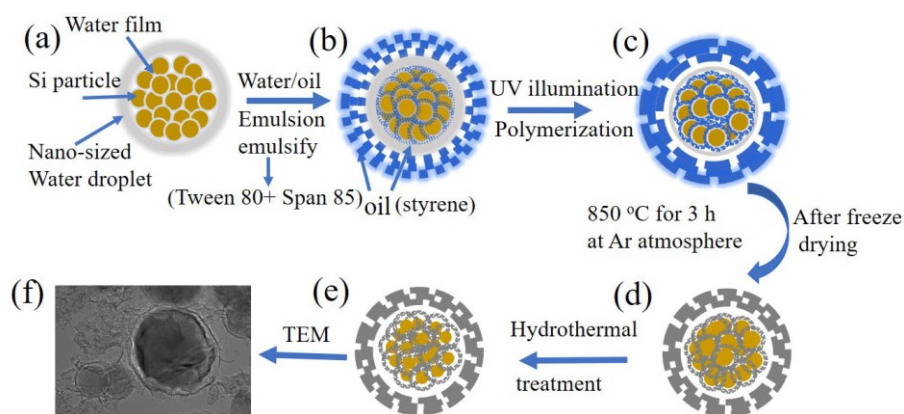
## 2. Results and Discussion

Figure 1 schematically presents the synthesis methodology of Si@void@C/C with yolk-shell structure embedded in 3-D porous carbon network. Commercial pure silicon particles (purchased from the company of Siping Changchun, China) were chosen as the starting materials. Owing to the positive charge from the Si particles,<sup>[23,24]</sup> the synthesis process takes advantage of hydrophilicity of silicon powder (Figure 1a and Figure S1a in Supporting

Information (SI)). First, in the water/oil system (Figure 1b), the added (3-Aminopropyl) triethoxysilane coupling agent is compatible with organic substances (styrene monomer acted as oil phase). The other end of the molecules chain of the (3-Aminopropyl) triethoxysilane coupling agent would be hydrolyzed to yield Si-OH<sup>-</sup>, which is wielding repulsive influence on the silicon powders surrounded by water film. The UV illumination (Figure 1c) is employed to realize polymerization. With freeze-drying technique, all the water is removed to form void spaces. After calcination, see Figure 1d and Figure S1b, there are more spaces left in the hybrid compound. Owing to the oxide layer on pure Si powder, the enhanced activity of silicon atoms on the surface of SiO<sub>2</sub> could make it easier to bond Si with hydroxyl groups to form Si(OH)<sub>5</sub><sup>-</sup> under the hydrothermal conditions. This reaction results in the rapid dissolution of amorphous SiO<sub>2</sub>. As the reaction goes on, Si powders may follow up with a weak chemical reaction under the high temperature and the high pressure of hydrothermal condition:



In addition, the bond Si-C also can be corrosioned by the hydrothermal treatment. All these factors make the water erode the Si and expand the space inside the carbon shell. Hydrothermal treatment further enlarges the void spaces by the water eroding Si (Figure 1e), that more void spaces are located between the carbon shell and Si particles. Figure 1f and Figure S1c reveal that the final product Si@void@C/C has yolk-shell structure with the large void space.



**Figure 1.** Schematic explanation of producing yolk-shell Si@void@C/C methodology

In order to verify the crystalline phase and the existence of carbon for as-prepared Si-carbon nanocomposites, pure Si powders and Si@void@C/C-2 samples were measured by X-ray

diffraction (XRD) and Raman spectroscopy technologies. As shown in Figure 2a, the peaks of samples located at 28.5, 47.4, 56.2 and 69.2 degrees, can be well-traced to (111), (220), (311) and (400) planes (JCPDS 27-1402).<sup>[25]</sup> Compared to pure Si, the broad peak at  $\sim 24^\circ$  is identified as amorphous carbon phase for Si@void@C/C-2.<sup>[26]</sup> Raman spectra were employed to further confirm the existence of carbon. Figure 2b displays the Raman spectra in the range from 400 to 1800  $\text{cm}^{-1}$  for Si@void@C/C-2 and pure Si samples. Four distinct peaks located at  $\sim 513$ , 923, 1354, and 1590  $\text{cm}^{-1}$ , respectively, are the characteristic peaks of Si and carbon.<sup>[27, 28]</sup> Carbon peaks are divided into a disorder band (D-band) at 1354  $\text{cm}^{-1}$  and an apparent graphitic band (G-band) at 1590  $\text{cm}^{-1}$ . The value of  $I_D/I_G$  is 0.987, indicating that the carbon shells and carbon nets have been partially changed into graphitic. The graphitic carbon can provide some unique merits during electrochemical reaction of the silicon anode in lithium ion batteries, such as high electric conductivity, stability for accommodating volume change, and strong synergetic effect with silicon for ultrafast charge and discharge rates.<sup>[29,30]</sup>

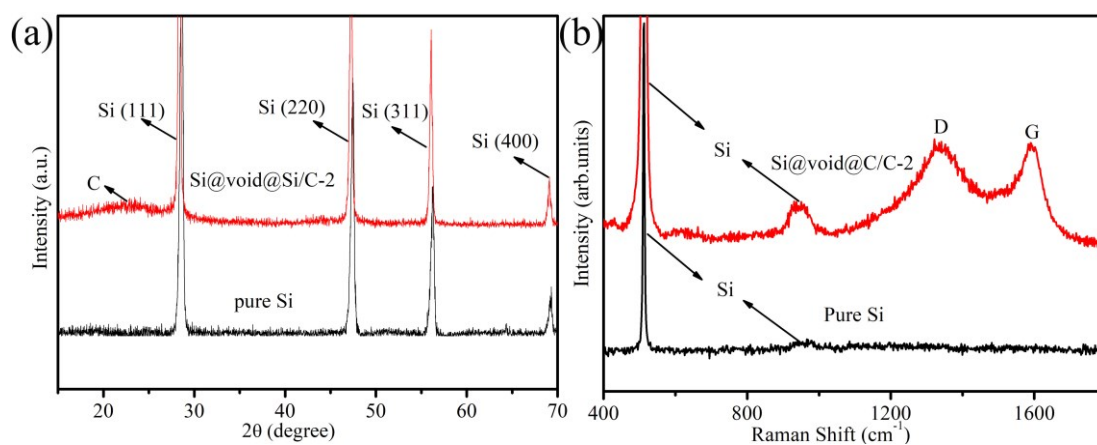


**Figure 2.** (a) XRD patterns and (b) Raman spectra of pure Si and Si@void@C/C-2.

The morphology and microstructure of samples were analyzed by scanning electron microscope (SEM) and transmission electron microscopy (TEM). Figure S2a reveals that the round pure Si powders clearly scattered in the vision with an average size from 50-200 nm. In the synthesis process, the UV illumination time plays a vital role in the polymerization degree of polystyrene and the detailed nanostructure of samples. Figure S2b shows the morphology of sample Si@void@C/C-1, corresponding to 1 h for UV illumination time. It clearly illustrates the monodispersed nanoparticles with the diameter of approximately 50-200 nm. When the

polymerization time up to 2 h for polystyrene, sample Si@void@C/C-2 displays Si@void@C embedded in large amount of carbon-based matrix (Figure S2c), which possesses a good mechanical-strength with three-dimensional carbon network architecture. However, when the polymerization time prolong to 3 h, sample Si@void@C/C-3 shows that the Si nanoparticles are completely inundated by carbon base materials, see Figure. S2d. As the UV illumination time increases, the microstructures of samples also present regular variation. Figure S3 shows the N<sub>2</sub> adsorption-desorption isotherm and the pore size distribution of three samples. There is a sharp rise in low relative pressure ( $P/P_0 < 0.01$ ) region for sample Si@void@C/C-1, which is the evidence of the existence of micropores. The obvious hysteresis peak at high relative pressure for Si@void@C/C-2 and Si@void@C/C-3 indicates the existence of mesopores and macropores (Figure S3a). However, Figure S3b displays that all samples have the dominant mesoporous characteristic structure. Compared to the other two samples, there are micropores located inside of sample Si@void@C/C-1 with high quantity of nitrogen, see Figure S3 c. With the increase of UV illumination time, the BET surface area of the final product displays decreased tendency. The micropore size distribution of Si@void@C/C-1 in Figure S3 d shows the micropore size centered at 1.5-2 nm. The detail data of Si@void@C, Si@void@C/C-1 and Si@void@C/C-2 are 156.2, 76.8 and 37 m<sup>2</sup> g<sup>-1</sup>, respectively. Owing to the porous skeleton of Si@void@C/C is blocked by the more polymerized thermal decomposed carbon, the BET surface area of Si-carbon composition significantly decreases with the carbon content increased.

[31]

In Figure S4a, thermogravimetric (TG) measurement shows the mass percentages of carbon in porous Si/C nanocomposites. It was carried out under air atmosphere from 45 to 850 °C to explore the carbon effect on battery performance triggered by different weight ratios of carbon. As shown in Figure S4a, at an initial stage (45-200°C) of TG profile, the weight loss comes from the adsorbed water. As the increasing of temperature (under 200 - 400 °C), one can see an increase of line data in the profile ( $\text{Si} + \text{O}_2 \rightarrow \text{SiO}_x$ ), which is owing to Si nanoparticles oxidation in air. The large and fast weight loss after 400 °C is ascribed to the carbon decomposition. The analysis of TG curves shows the carbon content for Si@void@C/C-1, Si@void@C/C-2 and Si@void@C/C-3, are approximately 10.1 %, 24.2 % and 25.5 %, respectively.

The chemical compositions and the binding energy of chemical bonding for Si/C nanocomposite were assessed by X-ray photoelectron spectroscopy. In Fig. S4b, the wide XPS spectrum for sample Si@void@C/C-2 shows the characteristic peaks of Si 2p, Si 2s, C1s, and O 1s at 103.1 eV, 283.9 eV and 539.67 eV, respectively. In Figure S4c, three peaks located at 103.8 eV, 103.2 eV and 99.1 eV in Si 2p region, are traced to silicon oxides (SiO<sub>x</sub>) and pure Si.<sup>[32, 33]</sup> The oxidation states indicate the instability of Si nanoparticles during UV illumination and hydrothermal synthesis. It's worth noting that the thin SiO<sub>x</sub> layer reacts with Li<sup>+</sup> ions, forming Li<sub>2</sub>O and lithium silicates to buffer the volume change and improve the cycling stability of Si yolk particles under charge/discharge process.<sup>[34, 35]</sup> In Figure S4d, the four peaks can further confirm the existence of C1s. The peaks at 283.65 eV and 283.55 eV are assigned to C-Si bond, suggesting the formation of free carbon.<sup>[36]</sup> The 284.8 eV is associated with the graphite-like sp<sup>2</sup> hybridized carbon, the other peak at 286.4 is coordinated with C-O bonds of carbon composition.<sup>[37]</sup>

To explicitly distinguish the yolk-shell structure of Si@void@C and the interconnected 3D porous architecture, the TEM images were collected to explore the outside and inside of structural morphology for the samples. As shown in Figure 3a, it displays a very clear yolk-shell structure of Si@void@C particles hybrid with carbon together. Figure 3b shows that Si@void@C nanoparticles with size of 100 -200 nm, are distributed among the cross-linked carbon network. Such a sponge-like carbon net around the Si@void@C particles can effectively buffer the mechanical strain during charge/discharge cycling of active Si component, maintain a robust electronic conducting pathway, and ensure a stable SEI layer on the outer surface of carbon net.<sup>[38]</sup> A detailed microstructure is depicted in Figure 3c. There is a distinct void space located between carbon and Si nanoparticles, evidencing the yolk-shell nanostructure. The marked lattice spacing distance of 0.31 nm matches well with (111) crystal plane. Because of the high specific surface area, Si nanoparticles have relatively reactive properties that make the oxidation easier when exposed to air. Thus, there is a thin layer of amorphous SiO<sub>x</sub> covered on the surface of Si particles. The amorphous oxidation layer combined with Si yolk particle can exhibit a cushioning effect and synergistic effect on the electrode structure during the discharge/charge process.<sup>[39,40]</sup> Figure 3d is an image from scanning transmission electron

microscopy (STEM) which is also employed to do Energy-dispersive X-ray spectroscopy (EDX) elemental mapping, see Figure 3e and Figure 3f. One can clearly observe the existence of carbon, void and carbon net covering the silicon nanoparticles well, demonstrating Si@void@C particles embedded in the cross-linked carbon network. In literature, it has been reported that carbon frameworks hosting Si can form a valid structure of Si anodes for enhanced electric conductivity to accommodate volume variation and contribute to a stable SEI.<sup>[41]</sup> The introduction of carbon can contribute to form the unique structure for Si@void@C/C samples. The defects of carbon nets and carbon shell provide a pathway for the transmission of Li ions, and their passivation could also protect Li metal.<sup>[42]</sup>

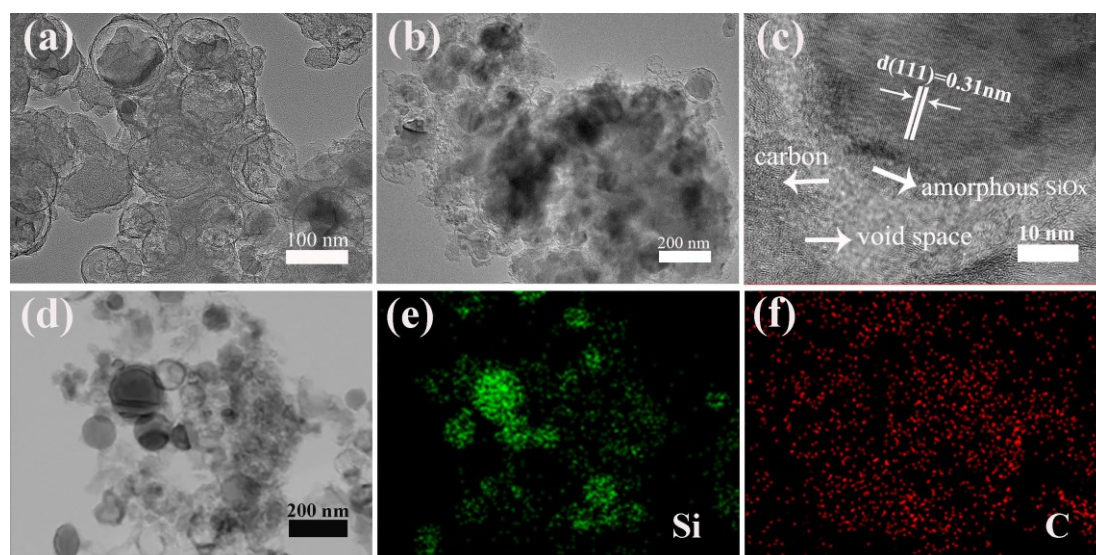


**Figure 3.** TEM images: (a) Si@void@C/C-1, (b) Si@void@C/C-2, (c) the corresponding HRTEM images of Si@void@C/C-1, (d) STEM image of Si@void@C/C-1, and corresponding elemental mapping of (e) Si and (f) C.

The well interconnected 3D porous carbon network architecture of sample can provide excellent electrochemical performance. Figure 4 shows the electrochemical reactive behaviors of sample Si@void@C/C-2 during charge-discharge acted as anodes for lithium ions. Figure 4a is the cyclic voltammetry (CV) curves of the first three cycles measured at  $0.1 \text{ mV s}^{-1}$  between 0.01 and 3.0 V for Si@void@C/C-2 electrode. The cathodic peaks located at  $\sim 0.72 \text{ V}$  and  $\sim 0.18 \text{ V}$  in the first CV curve are attributed to SEI formation and the formation of  $\text{Li}_x\text{Si}$  phase during cycling.<sup>[43]</sup> However, the reduction peaks  $< 0.1 \text{ V}$  are corresponding to the lithiation of graphite

carbon. In the next anodic scan, there are two anodic peaks centered at  $\sim 0.34$  V and  $\sim 0.48$  V, indicating de-alloying from  $\text{Li}_x\text{Si}$  to Si. Compared to the following cycling CV curves, it is found that the further activation and electrode wetting by electrolyte can prompt the intensity of the characteristic redox peaks growth with the cycling process.<sup>[44, 45]</sup> Figure 4b shows the 1st, 50th, 200th and 300th charge/discharge voltage vs capacity profiles of Si@void@C/C-2 anode under the current density of  $200 \text{ mA h g}^{-1}$ . In the initial discharge stage, there is a flat and long voltage plateau below 0.11 V caused by lithium insertion into the Si nanoparticles. The corresponding discharge capacity is  $2317 \text{ mA h g}^{-1}$  with the initial coulombic efficiency (CE) of 65.8%, where the irreversible SEI layer leads to its reversible capacity loss after the 1st cycle. In the charge process from 0.28 to 0.66 V, a sloping plateau can be observed, which is related to lithium ions extracted from the reactive materials. In the following cycles, from 50th cycle to 300th cycle, the Si@void@C/C-2 electrode maintains steady cycling capacity. Figure 4c and Figure 4d also provide evidence that the peculiar void space and 3D cross-linked carbon network can guarantee Si@void@C/C anode a good electrochemical performance. All cycling data are obtained with current density of  $200 \text{ mA g}^{-1}$  and potential range of 0.01 - 3.0 V. Figure 4c reveals that the capacity of commercial pure electrode rapidly goes down to  $62 \text{ mA h g}^{-1}$  after 55 cycles because of the huge volume change derived from cracking and expansion effect during lithium ions insertion and extraction, without the assistance of void space and carbon-based materials, which intrigue the structure damage.

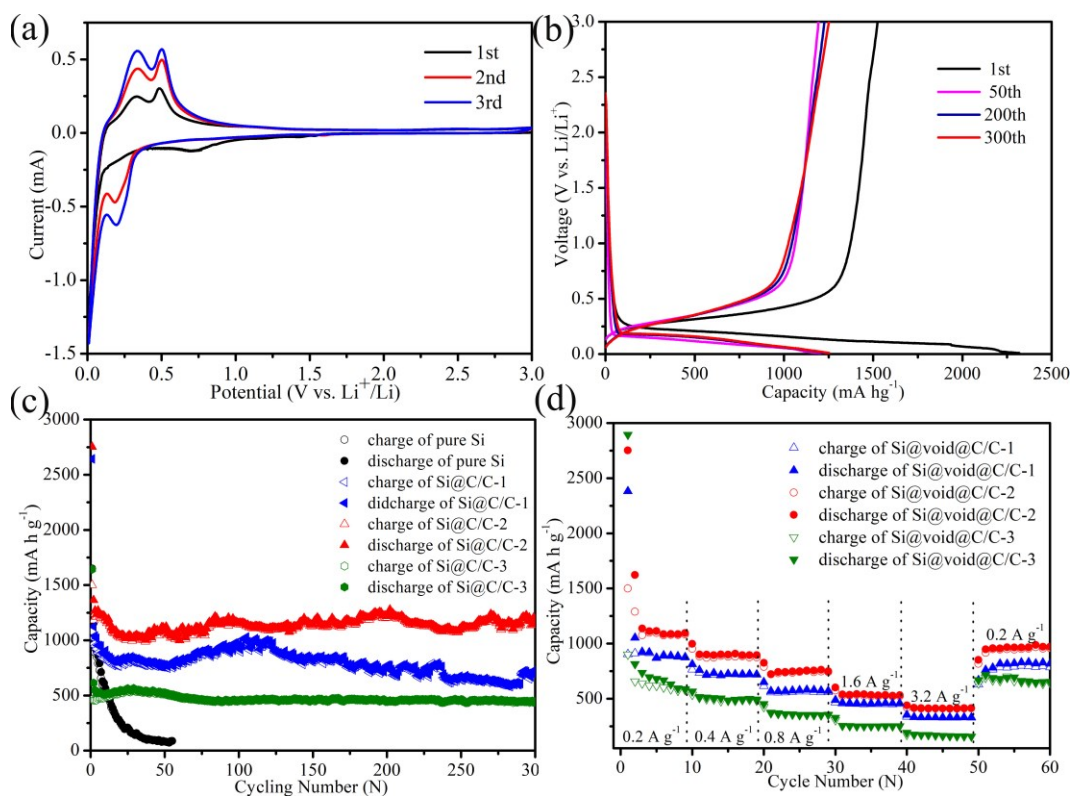


**Figure 4.** (a) Cyclic voltammetry curves of Si@void@C/C-2 for the first three cycles at a scan rate of  $0.1 \text{ mV s}^{-1}$  and (b) Voltage-capacity curves at a galvanostatic current density of  $200 \text{ mA g}^{-1}$  while cycling between  $3.0\text{-}0.01 \text{ V}$  vs  $\text{Li/Li}^+$  for electrode Si@void@C/C-2; (c) Cycling performance for the current density of  $200 \text{ mA g}^{-1}$ ; (d) Rate performance for Si@void@C/C-1, Si@void@C/C-2 and Si@void@C/C-3 composite electrode.

For Si@void@C/C-1 anode, the capacities in discharge after 20th, 120th and 300th cycle are  $815$ ,  $990$  and  $700 \text{ mA h g}^{-1}$ , respectively. In the initial 20 cycles, the appearance of SEI film decreased the reversible capacity, producing an inclined cycling tendency. After 20 cycles continuous activation, the anode shows increasing capacity until 120 cycle, followed by a decreasing trend in capacity. This capacity change may be resulted from the structure volume expansion of Si@void@C/C-1 anode. For sample Si@void@C/C-2, the capacity presents a fast decline in the first 20 cycles, and finally reaches a stable state with a capacity of  $1023 \text{ mA h g}^{-1}$  and related CE of 98%. In the subsequent cycles, the capacity is increased to  $1160 \text{ mA h g}^{-1}$ . The increase in capacity of the composite electrode is mainly due to the special architecture with yolk-shell Si@void@C nanoparticles embedded in 3D carbon network, which can delay

contact between the active material and the electrolyte. As reported in literature that the appropriate amount of carbon for Si@void@C/C-2 can increase the cyclable capacity and stability of nanocomposite electrode.<sup>[46]</sup> For sample Si@void@C/C-3 anode, comparing with sample Si@void@C/C-2, it exhibits a well stable cycling feature with a capacity of 450 mA h g<sup>-1</sup> after 300 cycles. Owing to Si@void @C nanoparticles are completely covered by the higher density carbon network in sample Si@void@C/C-3 anode (see Figure S1d), which couldn't get enough electrolyte under charge/discharge process. This obstructs the storage of Li<sup>+</sup> and growth of SEI of sample Si@void@C/C-3 anode, however, the cycling stability has been improved.

The rate capabilities of Si@void@C/C-1, Si@void@C/C-2 and Si@void@C/C-3 are evaluated under stepwise current densities from 200 mA g<sup>-1</sup>, 400 mA g<sup>-1</sup>, 800 mA g<sup>-1</sup>, 1600 mA g<sup>-1</sup> to 3200 mA g<sup>-1</sup>, as shown in Figure 4d. With the help of void space and suitable carbon network structure, Si@void@C/C-2 delivers reversible capacities of 1135 mA h g<sup>-1</sup> at 200 mA g<sup>-1</sup>. When the current density increased to 400 mA g<sup>-1</sup>, 800 mA g<sup>-1</sup>, 1600 mA g<sup>-1</sup> and 3200 mA g<sup>-1</sup>, it exhibits excellent reversible capacities of 892, 745, 530 and 410 mA h g<sup>-1</sup>, respectively. While the current density is set back to 200 mA g<sup>-1</sup>, the capacity can maintain 970 mA h g<sup>-1</sup>. All the reversible capacity of Si@void@C/C-2 anode is higher than the other samples under various current density. The outstanding rate capability and the high kinetic property for Si@void@C/C-2 electrode with 3D interconnected carbon-net are attributed to the void space, carbon shell and carbon-net that provide short pathway for electron and Li ions transmission.

The void space and unique 3D interconnected network features of Si@void@C/C not only can help to ensure the stress buffering for Si particles volume variation during electrochemical reactive process, but also facilitate electron transport. Electrochemical impedance spectroscopy of samples is employed to show conductivity behavior, shown in Figure 5a. One can see from the plots that the diameter of semicircle for Si@void@C/C-2 electrode at high frequency is the smallest. This means that the 3D interconnected carbon-net can provide a lower and stable interfacial resistance and effectively enhance the conductivity of the silicon-based materials.<sup>[47,48]</sup> As shown in Figure 5b, Si@void@C/C-2 electrode is activated by current density of 0.4 A g<sup>-1</sup>, followed by the current density of 1.0 A g<sup>-1</sup>. The anode can still maintain 480 mA h g<sup>-1</sup> charge capacity after 1000 cycles, which is 1.29 times higher than the theoretical

capacity of artificial graphite ( $372 \text{ mA h g}^{-1}$ ). The good prolonged cycle performance of Si@void@C/C-2 is primarily ascribed to the suitable void space distribution, dense carbon coating layer and 3D interconnected carbon network-like nanostructure. This unique structure can suppress pulverization of the active material, enhance the electron transferring conductivity and improve the electrochemical performance.<sup>[49,50]</sup>

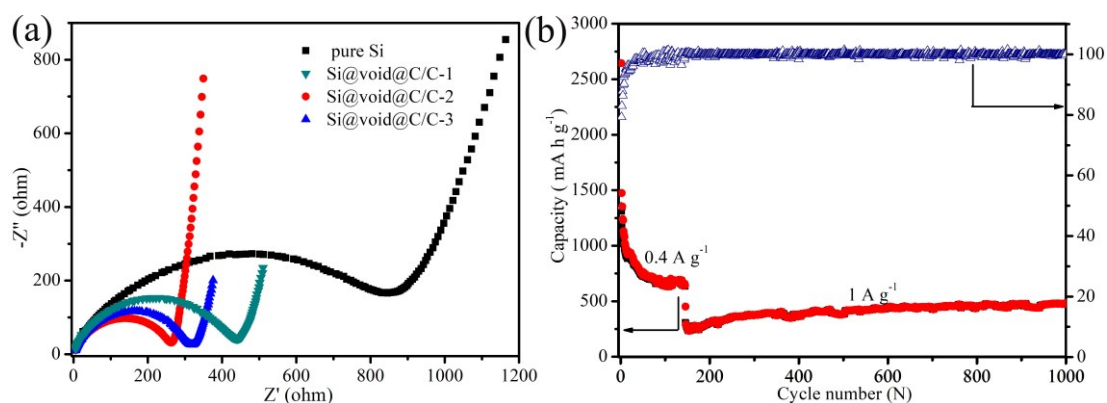


**Figure 5.** (a) Electrochemical impedance spectra for the pure Si nanoparticles, Si@void@C, Si@void@C/C-1 and Si@void@C/C-2 composite electrodes. (b) Long cycling performance and corresponding Coulombic efficiency (CE) for Si@void@C/C-2 at the current densities of  $1 \text{ A g}^{-1}$ .

Si@void@C/C-2 anode also shows superior specific capacity and cycling stability, see the comparison with other materials in table 1. In addition to the high capacity, the structure design for Si@void@C/C could realize industrial large scalable production. Moreover, the water-in-Oil system and hydrothermal process can lead to an economical and environmentally friendly development results.

**Table 1.** The comparison of cycling performance of Si@void@C/C anode with other reported materials

Sample material	Charge capacity (mAh g <sup>-1</sup> )	Current density (mAh g <sup>-1</sup> )	Method	Reference
Hollow Si@C Core-shell	700 (100 <sup>th</sup> )	250	HF-Si	[51]
Si@SiO <sub>2</sub> /C Yolk-shell	760 (100 <sup>th</sup> )	100	HF-SiO <sub>2</sub>	[52]
Si@void@C Yolk-shell	751 (100 <sup>th</sup> )	100	HF-SiO <sub>2</sub>	[53]
Si/C	1113 (200 <sup>th</sup> )	100	Spry-drying	[54]
Si@void@C/C	1160 (300 <sup>th</sup> )	300	Water-in-Oil	our work

In order to demonstrate the practical applicability of Si anodes, we assembled full cells with LNMC (Li(Ni<sub>1/3</sub>Mn<sub>1/3</sub>Co<sub>1/3</sub>)O<sub>2</sub>) as cathode. The practical cycling performance of the full cell is measured with a voltage window range from 2.2 to 4.6V. As shown in Figure 6, the cycle stability and the capacity of full cell increase with the cycle numbers. Figure. 6a shows that the first CE of full cell only has 62.3% with reversible capacity of 92 mA h g<sup>-1</sup> at 0.2 A g<sup>-1</sup>. As cycle goes on and the formation of SEI, CE stabilized at 99.2% until 15th cycle. Then the electrochemical activation process of whole cell materials pushes its capacity from 92 to 128 mA h g<sup>-1</sup> after the 1100th cycle, which is comparable to those of reported full cells based on Si anodes.<sup>[28, 37, 55]</sup> Three porous yolk-shell Si@void@C particles embedded in carbon nets, that continues nanostructure does not completely make electrolytes wetting the inside of Si particles in the initial 1000 cycles. After 1100 cycles, as the electrolyte gradually permeates, the smooth SEI films could be clearly observed on the surface of Si@void@C particales. Well-preserved integrity of the assembled anode material and the SEI films of Si@void@C particales could afford an excellent cycle life and rate ability under deep charge/discharge cycling.<sup>[56,57]</sup>

After 1100 cycles, Si@void@C anodes still keep the original spherical morphology embedded in interconnected three-dimensional (3-D) porous carbon architecture, see in Figure 6b. This well-preserved integrity of the assembled anode material can improve its long cycling stability and rate ability. SEM analysis in Figure. 6c also shows that there is no cracks and distinct fracture surface found in the cycled sample Si@void@C/C-2 electrode and SEI layer is maintained in a stable state. In addition, SEM images in Figure S5 show the cross section of Si@void@C/C-2 electrode before cycling and after 1100th cycle. The thickness of the electrode before cycling is 36  $\mu\text{m}$  in Figure S5a. After 1100th cycle, integrity structure of Si@void@C/C-2 electrode is still maintained within the architecture. Volume changes just increase the thickness of the electrode to 42.1  $\mu\text{m}$  in Figure S5b. The changed part is derived from the growth of SEI interphase located between active electrode and electrolyte. After repeated charging/discharging, the electrolyte begins to decompose due to the irreversible reaction among active electrode and the organic electrolyte. In literature the SEI film presents more porous and loose structure.<sup>[58]</sup> This structure is not only facilitating ions diffusion, but also isolating the electrode from the electrolyte, preventing the further decomposition of electrolyte.<sup>[59]</sup> However, there is no obvious shrinkage on the surface of the active materials. It is demonstrated that yolk-shell Si@void@C embedded in interconnected 3D porous carbon network architecture can completely withstand the volume changes during charging/discharging process, which is a very good mechanical resilient property. It is indicated a good cohesion between the Si@void@C particles and conductive carbon networks. This stabilized structure may be ascribed to the unique integrated Si@void@C/C-2 nanostructure with robust yolk-shell structure providing void space and polymer pyrolyzed carbon network on buffering additional volume changes by carbon shell, as well as stabilized SEI layer by outer 3D carbon network.<sup>[60,61]</sup>

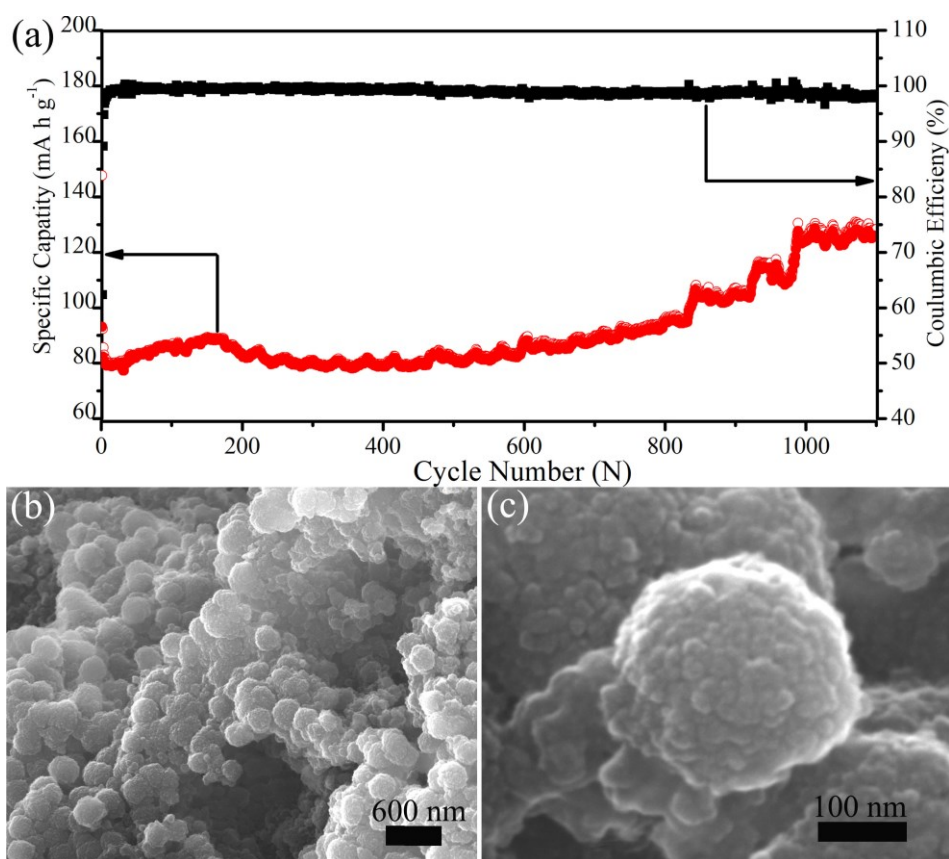


**Figure 6.** (a) Cycling performance for a Li(Ni<sub>1/3</sub>Mn<sub>1/3</sub>Co<sub>1/3</sub>)O<sub>2</sub> (LNMC)/silicon composite cell at 1C rate between 2.2 and 4.6 V. (b, c) SEM images of the Si@void@C/C-2 electrode after 1100 cycles on the full cell.

Based on the excellent electrochemical impedance, cyclic voltammetry, rate capability and excellent ultralong-life performance analysis of Si@void@C/C-2 electrode, the enhanced ionic and electronic conductivity must be ascribed to the yolk-shell Si@void@C embedded in interconnected three-dimensional (3-D) porous carbon network architecture. To be specific, yolk-shell and porous network architecture can greatly shorten the Li<sup>+</sup> diffusion and electron conductivity path, resulting in higher electrochemical performance of the anode materials. The void space and open porous network in the 3D Si@void@C/C can buffer the crystal structure variations induced by repetitive Li<sup>+</sup> intercalation/de-intercalation and avoid the stress-induced microcracks. In addition, the silicon nanocrystals and the excessive space or channels can play vital roles in suppressing the propagation of the micro-cracks to sustain 1100 discharging/charging cycles and even beyond. Consequently, both the ion/electron transferring and the cycling stability of the 3D Si@void@C/C anode are greatly enhanced.

### 3. Conclusions

In summary, we have demonstrated that the Water-in-Oil Micromulsion irradiated by UV illumination combined calcination and hydrothermal to modified industrial pure Si to synthesize yolk-shell Si@void@C embedded in interconnected 3D porous carbon network architecture. Yolk-shell nanostructure, void space and interconnected 3D porous carbon network can ensure the high electrons/ions transmit speed and decreased cracks of expansion/contraction for volume change under lithium ions insertion /extraction for Si-based active electrode. The results of electrochemical property reveal that sample Si@void@C/C-2 anode has a reversible capacity of 1160 mA h g<sup>-1</sup> at 0.2 A g<sup>-1</sup> after 300 cycles. When the cycle life prolonged to 1000 cycle, this novel electrode shows 480 mA h g<sup>-1</sup> at 1A g<sup>-1</sup>. While it assembled within LNMFC/silicon full battery, it has demonstrated a lithium ions capacity of 128 mA h g<sup>-1</sup>, an impressive cycling stability after 1100th cycles. This work reports a scalable, facile and low-cost process for commercial application process with Si-based anode electrode, which can also be extended to fabricate other materials with the large volume expansion (such as core-shell Sn@C, Ge@C, transition-metal oxides@C embedded in 3D porous carbon) for other related energy applications fields.

### 4. Experimental Section

Materials: Si nano-powders (50-200 nm), styrene (C<sub>6</sub>H<sub>5</sub>CH, AR), Tween-80 (C<sub>24</sub>H<sub>44</sub>O<sub>6</sub>, CP), Span 85 (C<sub>100</sub>H<sub>188</sub>O<sub>28</sub>, CP), (3-Aminopropyl) triethoxysilane (C<sub>9</sub>H<sub>23</sub>NO<sub>3</sub>Si, 99%), diphenyl phosphine oxide (C<sub>12</sub>O<sub>11</sub>OP, 98%).

Synthesis of Si@void@C/C powders: First, a nonionic surfactant with appropriate proportion of Tween 80 and Span 85 (the volume ration = 1:3) and 30 ml styrene monomer were chosen as oil phase. Then, the three contents were blended together by stirring. 1.0 ml (3-Aminopropyl) triethoxysilane coupling agent and 0.015 g diphenyl phosphine oxide photosensitizer were put into oil phase solution by turn, respectively. At the same time, moderate commercial pure Si powders with the purity of 99.99% were dissolved in 12 ml deionized water solution by ultrasonication for 10 minutes. In the following step, the precursor of Si powder solution mixed with oil phase contained styrene monomer solution to form water in oil emulsion by emulsifying

machine for 2 hours. Finally, under the UV illumination, styrene monomers (oil phase) were polymerized into polystyrene as carbon source. A gray black product can be obtained by carbonizing at 850 °C in Ar for 3 h and the hydrothermal treatment at 160 °C for 18 h. With the different UV illumination duration (1-3h), three samples were synthesized with different carbon content, and denoted as Si@void@C/C-1, Si@void@C/C-2 and Si@void@C/C-3.

#### Material characterization

The crystal structure, surface morphology and the crystal lattice of the prepared products were characterized by X-ray diffraction (XRD: Rigaku D/Max-KA, Cu Ka), field emission scanning electron microscopy (FESEM: SU-70), and the high-resolution transmission electron microscopy (HRTEM: JEM-2100F, 200 kV). The chemical components of the products were measured with an energy dispersive X-ray spectrometer (EDS). Nitrogen adsorption-desorption isotherms were determined by Gold APP V-Sorb 2800 surface area and porosity analyzer at 77 K. The specific surface area measurements, pore size distribution and total pore volume were calculated by the adsorption-desorption isotherm and the Barrett-Joyner-Halenda (BJH) method. X-ray photoelectron spectroscopy (XPS, ESCALAB 250 with 200 W Al Ka probe beam) was used to elucidate the electronic states of surface chemical composition for the samples.

#### Electrochemical measurements

The active material, acetylene black, and a sodiualginate binder were mixed at a weight ratio of 70:20:10 and dispersed in water solution to form slurry. The slurry was coated on copper foil and dried in a vacuum oven at 80 °C overnight prior to coin-cell assembly. Then cut it into round geometrical shape with a diameter of 12 mm. The mass of active materials used for electrochemical study was about 1.0 mg cm<sup>-2</sup>. The cells (CR2032 type coin cells) were assembled in a glove box with ultra-high purity argon and using polypropylene membrane (UBE Industries Ltd.) as the separator, Li metal as the counter electrode, and 1 M LiPF<sub>6</sub> in ethyl carbonate/dimethyl carbonate (EC/DEC) (1:1 v/v) as the electrolyte. To investigate the cycling stable features for Si@void@C/C electrode in full cell, the commercial LMNC was chosen as the cathode. The active material was coated on aluminium foil with the quantity loaded of the LMNC electrode to Si@void@C/C-2 anode as 5:1. The prepared and assembled process for the full cell was the same as the fabrication of half cell, with initial prelithiation for Si@void@C/C-

2 anode using half cells at  $0.2\text{ A g}^{-1}$  for one cycle. After prelithiation, the half cells were disassembled, then the Si@void@C/C-2 and LNCM (provided by the commercial production) electrodes were combined into full cells. The charge and discharge performance of electrodes was performed at room temperature with different current densities between cut-off voltages of 0.01-3.0 V (vs.  $\text{Li}^+/\text{Li}$ ) using a Land CT2001A cell charge/discharge test instrument. The cyclic voltammetry (CV) curves and EIS spectrum were carried on a CHI660E electrochemical work station.

### Supporting Information

Supporting Information is available from the Wiley Online Library or from the author.

### Acknowledgements

We acknowledge support from the National Youth Science Foundation of China (No.: 51702177).

### Conflict of Interest

The authors declare no conflict of interest.

### References

- [1] Y. Ding, P. Cano, A. Yu, J. Lu, Z. Z. Chen. *Electrochem. Ener. Rev.*, **2019**, 2(1): 1-28.
- [2] L. Wood III, M. Wood M, J. Li, Z. Du, E. Ruther, A. Hays, N. Muralidharan, L. Geng, C. Mao, I. Belharouak, *Ener. Storage Mater.*, **2020**, 29: 254-265.
- [3] Y. Jin, B. Zhu, Z. Lu, N. Liu, J. Zhu. *Adv. Ener. Mater.*, **2017**, 7(23): 1700715.
- [4] Z. Luo, Q. Xiao, G. Lei, Z. Li, & C. Tang. *Carbon*, **2016**, 98: 373-380.
- [5] U. Rehman, H. Wang, A. Manj, W. Luo, & J. Yang. *Small*, **2019**: 1904508.
- [6] P. Li, G. Zhao, X. Zheng, X. Xu, C. Yao, W. Sun, & X. Dou. *Ener. Storage Mater.*, **2018**, 15: 422-446.
- [7] L. Sun, T. Su T, L. Xu, B. Du, *Phys Chem Chem Phys*, **2016**, 18(3): 1521-1525.
- [8] Z. Yi, N. Lin, Y. Zhao, W. Wang, Y. Qian, Y. Zhu, Y. Qian. *Ener. Storage Mater.*, **2019**, 17:

93-100.

- [9] F. Zhang, L. Wan, J. Chen, X. Li, X. Yan. *Electrochimica Acta*, **2018**, 280: 86-93.
- [10] J. Ryu, D. Hong, S. Choi, S. Park. *ACS nano*, **2016**, 10(2): 2843-2851.
- [11] T. Yoon, T. Bok, C. Kim, Y. Na, S. Park, S. Kim, *ACS nano*, **2017**, 11(5): 4808-4815.
- [12] T. Ma, X. Yu, H. Li, W. Zhang, X. Cheng, W. Zhu, X. Qiu. *Nano letters*, **2017**, 17(6): 3959-3964.
- [13] W. Cheng, L. Zhao, L. Wu, W. Ding, T. Hu, S. Meng, *Electrochimica Acta*, **2018**, 265: 348-354.
- [14] R. Liu, C. Shen, Y. Dong, J. Qin, Q. Wang, J. Iocozzia, S. Zhao, K. Yuan, C. Han, B. Li, Z. Lin. *J. Mater. Chem. A*, **2018**, 6(30): 14797-14804.
- [15] X. Zhang, R. Guo, X. Li, L. Zhi. *Small*, **2018**, 14(24): 1800752.
- [16] J. Xie, L. Tong, L. Su, Y. Xu, L. Wang, Y. Wang. *J. Power Sources*, **2017**, 342: 529-536.
- [17] X. Zhang, D. Kong, X. Li, L. Zhi. *Adv. Func. Mater.*, **2019**, 29(2): 1806061.
- [18] Y. Zhang, Z. Mu, J. Lai, Y. Chao, Y. Yang, P. Zhou, Y. Li, Z. Xia, & S. Guo. *ACS nano*, **2019**, 13(2): 2167-2175.
- [19] X. Huang, D. Cen, R. Wei, H. Fan, Z. Bao. *ACS appl. mater. interfaces*, **2019**, 11(30): 26854-26862.
- [20] L. Yue, W. Zhang, J. Yang, L. Zhang. *Electrochimica Acta*, **2014**, 125: 206-217.
- [21] S. Guo, X. Hu, Y. Hou, Z. Wen. *ACS appl. mater. interfaces*, **2017**, 9(48): 42084-42092.
- [22] Kim S, Hwang C, Park S Y, Ko S J, Park H, Cho, J. Kim B, Kim D S, Park S, Kim J Y, Song H K, *J. Mater. Chem. A*, **2014**, 2(42): 18070-18075.
- [23] F. Wang, B. Wang, T. Ruan, T. Gao, R. Song, F. Jin, Y. Zhou, D. I. Wang, H. Liu, and S. Dou. *ACS nano*. **2019**, 13(10):12219-12229.
- [24] T. Ruan, B. Wang, Y. Yang, X. Zhang, R. Song, Y. Ning, Z. Wang, H. Yu, Y. Zhou, D. Wang, H. Liu, and S. Dou. *Adv. Mater.*, **2020**, 32(17): 2000151
- [25] K. Fu, Y. Lu, M. Dirican, C. Chen, M. Yanilmaz, Q. Shi, D. Bradford, X. Zhang. *Nanoscale*, **2014**, 6(13): 7489-7495.
- [26] H. Jiang, S. Wang, Y. Shao, Y. Wu, J. Shen, X. Hao. *ACS Appl. Ener. Mater.*, **2019**, 2(1): 896-904.

- [27] P. Fan, S. Lou, S. Sun, L. Wu, Z. Qian, T. Mu, Y. Y. Ma, X. Cheng, Y. Gao, P. Zuo, & C. Du. *Electrochimica Acta*, **2020**, 332: 135507.
- [28] P. Reddy, T. Puneetha, W. Lee, H. Jeong, C. Park. *Org. Electron.*, **2017**, 50: 435-442.
- [29] P. Nie, X. Liu, R. Fu, Y. Wu, J. Jiang, H. Dou, X. Zhang, *ACS Ener. Letters*, **2017**, 2(6): 1279-1287.
- [30] J. Liu, C. Wu, D. Xiao, P. Kopold, L. Gu, A. van Aken, J. Maier, Y. Yu, *Small*, **2016**, 12(17): 2354-2364.
- [31] M. Jiao, K. Liu, Z. Shi, C. Wang. *ChemElectroChem*, **2017**, 4(3): 542-549.
- [32] J. Guo, W. Zhai, Q. Sun, Q. Ai, J. Li, J. Cheng, L. Dai, L. Ci. *Electrochimica Acta*, **2020**, 342: 136068.
- [33] J. Li, W. Liu, Q. Wan, F. Liu, X. Li, Y. Qiao, M. Qu, G. Peng. *Ener. Tech.*, **2019**, 7(9): 1900464.
- [34] F. Zhang, G. Zhu, K. Wang, M. Li, J. Yang. *Chem. Commun.*, **2019**, 55, 10531-10534.
- [35] A. Su, J. Li, J. Dong, D. Yang, G. Chen. *Small*, **2020**, 2001714.
- [36] M. Zhu, J. Yang, Z. Yu, H. Chen, F. Pan. *J. Mater. Chem. A*, **2017**, 5(15): 7026-7034.
- [37] Y. He, G. Xu, C. Wang, L. Xu, K. Zhang. *Electrochimica Acta*, **2018**, 264: 173-182.
- [38] P. Nie, Z. Le, G. Chen, D. Liu, X. Liu, B. Wu, P. Xu, X. Li, F. Liu, L. Chang, X. Zhang, X. Lu. *Small*, **2018**, 14(25): 1800635.
- [39] H. Chen, S. Wang, X. Liu, X. Hou, F. Chen, H. Pan, F. Chen, H. Pan, H. Qin, K. Lan, Y. Xia, G. Zhou. *Electrochimica Acta*, **2018**, 288: 134-143.
- [40] L. Zhao, B. He, C. Li, K. Jiang, P. Wang, J. Ma, H. Xia, F. Chen, Y. He, Z. Chen, C. You, F. Kang. *J. Mater. Chem. A*, **2019**, 7, 24356-24365.
- [41] Y. Li, Q. Xu, G. Li, X. Yin, J. Wan, G. Guo. *Mater. Chem. Front.*, **2017**, 1(9): 1691-1708.
- [42] B. Wang, T. Ruan, Y. Chen, F. Jin, L. Peng, Y. Zhou, D. Wang, H. Liu, S. Dou. *Energy Storage*, **2020**, 24, 22-51.
- [43] J. Su, J. Zhao, L. Li, C. Zhang, C. Chen, T. Huang, A. Yu. *ACS appl. mater. interfaces*, **2017**, 9(21): 17807-17813.
- [44] Q. Li, L. Yin, J. Ma, Z. Li, Z. Zhang, A. Chen, C. Li. *Energy*, **2015**, 85: 159-166.
- [45] Z. Liu, X. Chang, T. Wang, W. Li, H. Ju, X. Zheng, X. Wu, C. Wang, J. Zheng, X. Li. *ACS*

*nano*, **2017**, 11(6): 6065-6073.

- [46] L. Zhang, J. Jiang, C. Zhang, B. Wu, F. Wu. *J. Power Sources*, **2016**, 331: 247-257.
- [47] X. Zhang, D. Kong, X. Li, L. Zhi, *Adv. Func. Mater.*, **2019**, 29(2): 1806061.
- [48] X. Liu, A. Iqbal, N. Ali, R. Qi, and X. Qian. *ACS appl. mater. interfaces*, 2020, 12(17): 19431-19438.
- [49] M. Chen, Q. Zhou, J. Zai, A. Iqbal. T-T, Tsega, B. Dong, X. Liu, Y. Zhang, C. Yan, L. Zhao, A. Nazakat, S-P. E, C-T-J, Low, and X. Qian. *Nano Res.*, **2020**, 1-8.
- [50] M. Chen, B. Li, X. Liu, L. Zhou, L. Yao, J. Zai, X. Qian, and X. Yu. *J. Mater. Chem. A*, **2018**, 6: 3022-3027.
- [51] T. Wang, H. Li, S. Shi, T. Liu, G. Yang, Y. Chao, & F. Yin. *Small*, **2017**, 13(20): 1604182.
- [52] C. Pang, H. Song, N. Li, C. Wang, *Rsc Adv.*, **2015**, 5(9):6782-6789.
- [53] S. Hu, R. Demir-Cakan, M. Titirici, O. Müller, R. Schlögl, M. Antonietti, J. Maier. *Angew. Chem. Int. Edi.*, **2008**, 47(9): 1645-1649.
- [54] Z. Jiao, Y. Gao, S. Liu, S. Huang, Y. Jiang, Z. Chen, B. Zhao, *Electrochimica Acta*, **2018**, 283: 1702-1711.
- [55] L. Hu, B. Luo, C. Wu, P. Hu, L. Wang, H. Zhang. *J. Ener. Chem.*, 2019, 32: 124-130.
- [56] X. Liu, J. Zai, A. Iqbal, M. Chen, Z. Ali, R. Qi, and X. Qian. *J. Colloid and Interface Science*, 2020, 565: 270-277.
- [57] H. Wu, G. Chan, C. Jang, Ryu III, Y. Yao, T, McDowell, W. Lee, A. Jackson A, Y. Yang, L, Hu and Y. Cui. *Nat. nanotech.*, **2012**, 7: 310-315.
- [58] C. Bao, B. Wang, P. Liu, H. Wu, Y. Zhou, D. Wang, H. Liu, and S. Dou. *Adv. Funct. Mater.*, 2020, 2004891.
- [59] Y. Jiang, B. Wang, P. Liu, B. Wang, Y. Zhou, D. Wang, H. liu, S. Dou. *Nano Energy*, **2020**, 77, 105308.
- [60] S. Chen, L. Shen, A. Aken, J. Maier, Y. Yu, *Adv. Mater.*, **2017**, 29(21): 1605650.
- [61] H. Ji, C. Ma, J. Ding, J. Yang, G. Yang, Y. Chao, & Y. Yang. *J. Power Sources*, **2019**, 413:42-49.